nature materials

ARTICLES

https://doi.org/10.1038/s41563-018-0242-y

Double-lattice photonic-crystal resonators enabling high-brightness semiconductor lasers with symmetric narrow-divergence beams

Masahiro Yoshida[1], Menaka De Zoysa[1], Kenji Ishizaki[1], Yoshinori Tanaka[1], Masato Kawasaki[1,2], Ranko Hatsuda[1], Bongshik Song[1,3], John Gelleta[1] and Susumu Noda[1]*

Achieving high brightness (where brightness is defined as optical power per unit area per unit solid angle) in semiconductor lasers is important for various applications, including direct-laser processing and light detection and ranging for next-generation smart production and mobility. Although the brightness of semiconductor lasers has been increased by the use of edge-emitting-type resonators, their brightness is still one order of magnitude smaller than that of gas and solid-state/fibre lasers, and they often suffer from large beam divergence with strong asymmetry and astigmatism. Here, we develop a so-called 'double-lattice photonic crystal', where we superimpose two photonic lattice groups separated by one-quarter wavelength in the *x* and *y* directions. Using this resonator, an output power of 10 W with a very narrow-divergence-angle (<0.3°) symmetric surface-emitted beam is achieved from a circular emission area of 500 μm diameter under pulsed conditions, which corresponds to a brightness of over 300 MW cm^{-2} sr^{-1}. In addition, an output power up to ~7 W is obtained under continuous-wave conditions. Detailed analyses on the double-lattice structure indicate that the resonators have the potential to realize a brightness of up to 10 GW cm^{-2} sr^{-1}, suggesting that compact, affordable semiconductor lasers will be able to rival existing gas and fibre/disk lasers.

The brightness B of laser beams is a figure of merit that expresses how intensely a laser beam can be focused, or how narrowly an emitted laser beam diverges, and is defined as

$$B = \frac{P}{S \times \Omega} \quad (1)$$

where P, S and Ω are the output power, emission area and solid angle of the emitted beam, respectively[1,2]. Semiconductor lasers with high brightness are in high demand for material processing and sensing (for example, light detection and ranging (LiDAR)) applications, which will be important for next-generation smart production and mobility in Society 5.0 (proposed by the Japanese government as a future society, http://www8.cao.go.jp/cstp/english/society5_0/index.html). Semiconductor lasers with various kinds of resonator have been developed over the years, but their brightness has been more than one order of magnitude smaller than those of existing gas and fibre/disk lasers[3–11]. The limited brightness is due to laterally multimode oscillation, which occurs when increasing the emission area S to increase B[12–17] (Supplementary Section 1). When a laser operates in a high-order lateral mode of order m in the x direction and order n in the y direction, its brightness B can be rewritten from equation (1) as

$$B \propto \frac{S}{(m+1)(n+1)} \quad (2)$$

Evidently, brightness decreases significantly when m or n increases. An increase in brightness is thus contingent on the ability of the laser to continue to operate in a single (or at least low-order) lateral mode following an expansion of S. Recently, ridge-waveguide edge-emitting lasers with 10 μm stripe widths specially designed to avoid the appearance of high-order modes have been developed, allowing a nearly diffraction-limited power of 1–2 W (corresponding to a brightness of 100–200 MW cm^{-2} sr^{-1}) to be achieved[18]. Separately, tapered edge-emitting lasers have shown an even higher brightness of ~1 GW cm^{-2} sr^{-1} (ref. [19]). However, these lasers have several undesirable features due to limitations inherent to their edge-emitting-type resonators. For example, these lasers have large beam asymmetry with a large beam divergence angle along the vertical direction. Such asymmetric beams with large beam divergence are unwieldy for most applications, requiring complicated optical systems for focusing the laser beam. Tapered lasers are particularly problematic in practical applications as they also have a significantly large astigmatism, which is highly dependent on the injection current. Due to this astigmatism, the emitted beam cannot be focused well with a simple lens and requires astigmatism-compensating complex optical systems.

Semiconductor lasers with surface-emitting-type resonators are favoured for overcoming these disadvantages of edge-emitting-type resonators. However, vertical-cavity surface-emitting lasers, where the resonator is formed from two vertically stacked distributed Bragg reflectors (DBRs), exhibit multimode operation once their resonator is widened beyond a few micrometres, and the brightness of these lasers remains small (1–5 MW cm^{-2} sr^{-1})[10,11,13]. On the other hand, surface-emitting lasers with photonic-crystal resonators[20–27], which operate in a mode of vanishing group velocity at the band-edge of a photonic crystal, show promise. Single-mode operation of one such laser over a broad 200 μm × 200 μm area has

[1]Department of Electronic Science and Engineering, Kyoto University, Kyoto, Japan. [2]Advanced Technology R&D Center, Mitsubishi Electric Corporation, Hyogo, Japan. [3]Department of Electrical and Computer Engineering, Sungkyunkwan University, Suwon, South Korea. *e-mail: snoda@kuee.kyoto-u.ac.jp

been reported[28] where the emission area S was more than 1,000 times larger than for conventional single-mode lasers. However, the single-mode output power was limited to the order of one watt (~0.5 W), which corresponds to a brightness of ~50 MW cm^{-2} sr^{-1}, above which high-order lateral modes appeared and the brightness degraded[28].

Here, we propose a photonic-crystal resonator that is capable of realizing an output power more than 10 times greater than previous photonic-crystal lasers, while achieving an even narrower and more symmetric beam divergence. This 'double-lattice' photonic-crystal resonator, as it will be called here, is composed of two distinct lattices separated in the x and y directions by one-quarter wavelength. This photonic crystal is capable of suppressing the oscillation of high-order modes over one order of magnitude more strongly than conventional, single-lattice ones, thereby enabling single- (or low-order) mode operation with emission areas 5–10 times broader than what was possible before. Using this approach we achieve output powers around 10 W with very narrow divergence angles of less than 0.3° in both x and y directions from a broad circular emission area of 500 μm diameter under pulsed conditions, which corresponds to a brightness of over 300 MW cm^{-2} sr^{-1}. In addition, an output power of up to ~7 W is obtained under continuous-wave (c.w.) conditions. Detailed theoretical calculations reveal the possibility of an optimized double-lattice photonic crystal reaching emission areas several tens to one hundred times broader than those of single-lattice photonic crystals, as well as brightnesses on the order of 1–10 GW cm^{-2} sr^{-1}.

Concept of double-lattice photonic-crystal resonators

General description. Figure 1a presents a schematic of a double-lattice photonic-crystal resonator. The photonic crystal is composed of two lattice point groups (indicated in black in Fig. 1b and in red in Fig. 1c). The red lattice points are shifted in the x and y directions by $d \approx 0.25a$ from the black points (a is the lattice constant and is approximately equal to the wavelength in the material, λ). This unique double-lattice structure produces the resonance effect, which is not observed in conventional single-lattice structures, as shown in the following.

First let us consider a single lattice, as shown in Fig. 1b, where a single elliptical hole with a low dielectric constant inside a high-dielectric semiconductor is periodically arranged with a periodicity of a in the x and y directions. We define here the change in dielectric constant relative to the high-dielectric background as $\varepsilon(x,y)$. As explained in Supplementary Section 2, $\varepsilon(x,y)$ can be expressed as a Fourier expansion using reciprocal lattice vectors $\mathbf{G}_{m,n} = \left(\frac{2\pi m}{a}, \frac{2\pi n}{a}\right)$:

$$\varepsilon(x,y) = \sum_{m,n} F_{m,n} \mathrm{e}^{\left\{j\left(\frac{2\pi m}{a}x + \frac{2\pi n}{a}y\right)\right\}} \quad (3)$$

where m and n are integers and $F_{m,n}$ are Fourier coefficients. This periodic system has a photonic band structure (Supplementary Fig. 1a), whose Γ_2-point band edges we consider for lasing. At these band-edges, four fundamental Bloch waves, R_x, S_x, R_y and S_y, are coupled to each other to form two-dimensional (2D) broad-area resonance; these couplings are induced by $\mathbf{G}_{m,n}$: 180° couplings are induced directly by $\mathbf{G}_{\pm 2,0}$ and $\mathbf{G}_{0,\pm 2}$, while 90° couplings are induced indirectly via a higher-order Bloch wave by a set of reciprocal lattice vectors. Respectively, the total strengths of 180° and 90° couplings are given by coefficients κ_{1D} (specifically, κ_{1D+} and κ_{1D-}; Supplementary Fig. 1c) and κ_{2D} (κ_{2D+} and κ_{2D-} and their complex conjugates; Supplementary Fig. 1d) [29,30].

Next, let us shift the entire lattice by d in the x and y directions (Fig. 1c). The dielectric function of this shifted system is simply $\varepsilon(x-d, y-d)$:

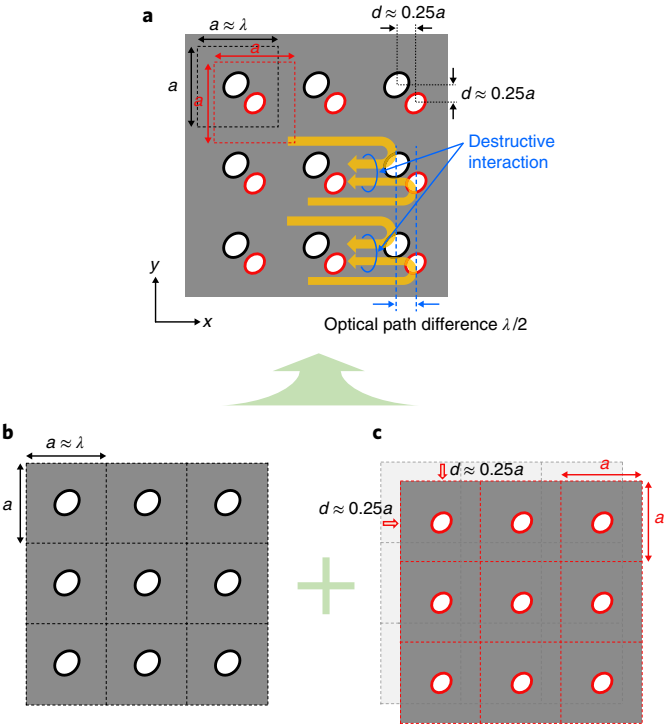

Fig. 1 | Double-lattice photonic-crystal resonators. a, Schematic of the double-lattice photonic-crystal resonator, which is composed of two lattice point groups (indicated in black and red). **b**,**c**, The individual lattice point groups, shown separately. The red lattice points are shifted by $d \approx 0.25a$ in the x and y directions from the black points, where the lattice constant a is set to the wavelength in the material, λ. Yellow arrows show the light waves, which are diffracted by 180° from each of the black and red lattice points and destructively interact with each other.

$$\begin{aligned}\varepsilon(x-d,y-d) &= \sum_{m,n} F_{m,n} \mathrm{e}^{\left\{j\left(\frac{2\pi m}{a}(x-d)+\frac{2\pi n}{a}(y-d)\right)\right\}} \\ &= \sum_{m,n} \mathrm{e}^{\left\{-j\left(\frac{2\pi m}{a}d+\frac{2\pi n}{a}d\right)\right\}} F_{m,n} \mathrm{e}^{\left\{j\left(\frac{2\pi m}{a}x+\frac{2\pi n}{a}y\right)\right\}}\end{aligned} \quad (4)$$

Then, let us combine an original and translated lattice to form our double-lattice structure (Fig. 1a). For simplicity, we consider the case in which the two lattices have air holes of identical shape. The dielectric function of this structure is the sum of equations (3) and (4), without approximation:

$$\begin{aligned}&\varepsilon(x,y) + \varepsilon(x-d,y-d) \\ &= \sum_{m,n} \left[1 + \mathrm{e}^{\left\{-j\left(\frac{2\pi m}{a}d+\frac{2\pi n}{a}d\right)\right\}}\right] F_{m,n} \mathrm{e}^{\left\{j\left(\frac{2\pi m}{a}x+\frac{2\pi n}{a}y\right)\right\}}\end{aligned} \quad (5)$$

Within this equation, the influence of combining two lattices, one of which is shifted by d from the other, is fully captured by the following term:

$$\left[1 + \mathrm{e}^{\left\{-j\left(\frac{2\pi m}{a}d+\frac{2\pi n}{a}d\right)\right\}}\right] \quad (6)$$

This term describes the mutual interaction between the two lattices, and represents the conceptual difference between the single- and double-lattice structures. As is evident from equation (6), the amplitude of each Fourier expansion term of the double-lattice

structure in equation (5) varies from 0 to 2 times those of the single-lattice structure in equation (3), depending on the values of m, n and d. Specifically, the amplitude evaluates to 2 when the binomial $\left(\frac{2\pi m}{a}d+\frac{2\pi n}{a}d\right)$ is an even-integer multiple of π; we call this situation a constructive interaction between the two lattices. On the other hand, the amplitude evaluates to 0 when $\left(\frac{2\pi m}{a}d+\frac{2\pi n}{a}d\right)$ is an odd-integer multiple of π; we call this situation a destructive interaction between the two lattices. Of course, the term may be finely adjusted between either extreme by a deliberate, straightforward selection of d.

In Fig. 1a, we consider the particular case when $d=a/4$. Substituting this value into equation (6) gives $\left[1+\exp\left\{-j\frac{\pi}{2}(m+n)\right\}\right]$. Inputting integers $(m,n)=(\pm2,0)$ and $(m,n)=(0,\pm2)$ into this term returns values of zero, which, when substituted into equation (5), implies that the strength of diffraction by vectors $\mathbf{G}_{\pm2,0}$ and $\mathbf{G}_{0,\pm2}$ disappears. In other words, the double-lattice structure eliminates direct 180° coupling among the four fundamental Bloch waves. Meanwhile, indirect 90° coupling is maintained as explained in Supplementary Section 2. In terms of the total coupling coefficients introduced above, the double-lattice structure reduces κ_{1D} and maintains κ_{2D}.

Consequently, the light spreads throughout the entire cavity area in a phenomenon we call 'flattening'. This flattening of the light increases the difference in optical loss between the fundamental and high-order cavity modes, because the anti-nodes of the high-order modes are closer to the edges of the cavity than the fundamental mode, and thus a greater portion of the higher-order mode energy leaks from the edges than the fundamental mode energy. In this way, the appearance of high-order modes is suppressed, and the stability of single- (or few-) mode operation is strengthened.

Specific examples. Figure 2a presents three examples of double-lattice photonic-crystal resonators with an air hole placed at each of their black and red lattice points. In structure I, the holes at the black lattice points (hereafter black holes) are larger than those at the red lattice points (hereafter red holes), and the black holes are also formed to a depth closer to the active layer than the red ones. In structure II, the sizes of the black and red holes are identical, but the difference in their depths is maintained. Finally, in structure III, the black and red holes have different sizes and shapes, but now their depths are identical, and also the separation between the black and red lattice points is finely tuned away from a distance of one-quarter wavelength so as to increase the effect of optical destructive interaction (section 'Optimized double-lattice photonic-crystal resonators'). The detailed structural parameters of structures I–III are provided in the caption of Fig. 2, and the role of in-plane and vertical asymmetry in diffracting light from the surface of the photonic crystal is described in Supplementary Section 3. The strength of 180° diffraction, κ_{1D} (the average of κ_{1D+} and κ_{1D-}) for each structure is as follows: I, ~470 cm^{-1}; II, ~250 cm^{-1}; III, ~100 cm^{-1}. Meanwhile, κ_{1D} of a conventional single-lattice structure is ~2,000 cm^{-1} (Supplementary Fig. 2).

Figure 2b shows the electric field distribution of the fundamental and first high-order modes of the single-lattice[28] and double-lattice (structures II and III) photonic-crystal resonators, where a circular resonator with a diameter of $L=200$ μm is considered. In the double-lattice resonators, the first high-order modes are found to be pushed toward the edges due to weakened 180° diffraction. As a result, the first high-order mode of each double-lattice structure (structures II and III) has much higher in-plane optical loss than that of the fundamental mode, and thus the threshold gains (α_{1st}) of the first high-order modes are much higher than that (α_{0th}) of the fundamental mode as well. The relative ease of oscillation of the fundamental mode over the high-order mode can be quantified by their threshold gain difference $\Delta\alpha$, which is defined as $\alpha_{1st}-\alpha_{0th}$. Figure 2c shows $\Delta\alpha$, calculated as a function of diameter L using 3D coupled-wave analysis[29,30] for structures I–III. $\Delta\alpha$ of a single-lattice photonic crystal[28] is also shown for reference. A comparison of the four structures reveals that $\Delta\alpha$ widens in proportion to the degree to which 180° diffraction is suppressed. Owing to the mismatched size of its two lattice points and hence its incomplete suppression of 180° diffraction, structure I (green line) exhibits the smallest widening of $\Delta\alpha$ among the double-lattice photonic crystals. By using air holes with identical sizes, 180° diffraction is further suppressed and $\Delta\alpha$ further widened, as shown by structure II (blue line). Finally, by tuning the lattice-group separation as an additional degree of freedom, 180° diffraction is suppressed further still to achieve an even wider $\Delta\alpha$, as shown by structure III (red line). Compared with the single-lattice photonic crystal (black line) at a diameter of 200 μm, structures II and III are capable of maintaining almost the same value of $\Delta\alpha$ at wider diameters of ~500 μm and 800 μm, respectively. Herein lies the advantage of double-lattice photonic crystals—they are capable of achieving stable single- (or low-order) mode resonance over emission areas 5–10 times wider than single-lattice ones, which according to equation (2) leads to a proportional increase in brightness.

Demonstration of double-lattice resonators

Pulsed operation. To demonstrate the importance of double-lattice photonic-crystal resonators for high-brightness laser operation, we first fabricated a device defined as structure II in Fig. 2. As is shown in Fig. 2c, this structure provides sufficiently stable resonance of a single mode up to $L\approx500$ μm. Accordingly, we fabricated a device with a circular active region of a 500 μm diameter. The device was fabricated as shown in Fig. 3a (for details see Methods). Top and cross-sectional scanning electron microscope (SEM) images of the fabricated photonic crystal are shown in Fig. 3b. Clearly, the sizes of the two air holes are the same, but their depths are different, in accordance with the design.

Figure 3c shows peak power versus peak injection current for the fabricated device during room-temperature, pulsed operation, where the pulse width and the repetition frequency were set to ~200 ns and 200 Hz, respectively. A maximum peak power exceeding ~10 W was successfully obtained at an injection current of ~25 A. The threshold current was ~2 A, and the slope efficiency was ~0.4 W A^{-1} (as indicated by the auxiliary dashed line). Figure 3d,e shows the near-field pattern (NFP) and far-field pattern (FFP), respectively, measured from 5 A to 25 A. It is seen in the NFP that coherent lasing occurred over the entire broad area of 500 μm. From this broad area, a single-spot beam with a very narrow divergence angle of less than 0.3° (evaluated using the beam's $1/e^2$ width) was emitted over the entire measured injection current range. Figure 3f shows the laser brightness evaluated using the measured NFP and FFP widths. A very high brightness exceeding 300 MW cm^{-2} sr^{-1} was obtained at a peak power of 10 W.

Continuous-wave operation. Next, we demonstrated the usefulness of double-lattice photonic-crystal resonators even under c.w. conditions by fabricating a second laser device with a double-lattice photonic-crystal resonator, defined as structure III in Fig. 2. Again, we set the device diameter to the maximum value, here 800 μm, at which $\Delta\alpha$ can be sufficiently large. This larger size will assist the dissipation of heat that naturally accumulates and degrades device performance during c.w. operation. In addition to expanding the device size, we introduced a DBR into the p cladding layer to serve as a back reflector. This DBR increased the slope efficiency and also alleviated the generation of heat by reflecting the downward light upward into the output beam.

The left panel of Fig. 4a is a top-view SEM image of the fabricated double-lattice photonic crystal using structure III. The right panel of Fig. 4a shows a cross-sectional SEM image along the A–A′ line

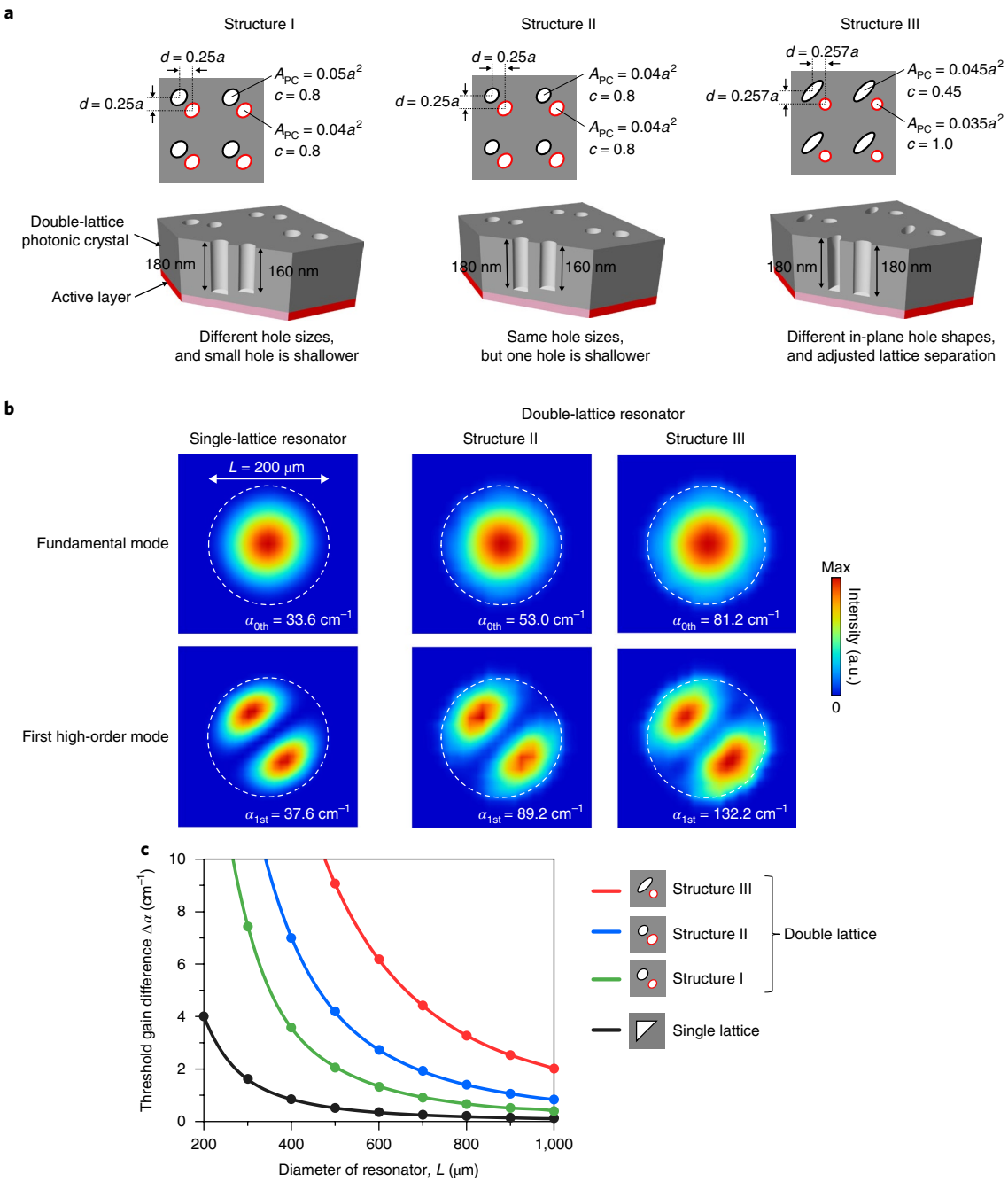

Fig. 2 | Examples of double-lattice photonic-crystal resonators and calculated mode stability. a, Top and cross-sectional views of three examples of double-lattice photonic crystals, where d is the separation between the two lattices, A_{PC} is the area of the air hole within the unit cell, c is the ellipticity of the air hole and h_{PC} is the height of the air hole. In structure I, the black holes are larger than the red holes, and also the black holes are formed to a depth closer to the active layer than the red holes: $d=0.25a$; black hole: $A_{PC}=0.05a^2$, $c=0.8$, $h_{PC}=180$ nm; red hole: $A_{PC}=0.04a^2$, $c=0.8$, $h_{PC}=160$ nm. Structure II has two holes with the same in-plane size but the same difference in depth as in structure I: $d=0.25a$; black hole: $A_{PC}=0.04a^2$, $c=0.8$, $h_{PC}=180$ nm; red hole: $A_{PC}=0.04a^2$, $c=0.8$, $h_{PC}=160$ nm. In structure III, the black and red holes have different sizes and shapes, but their depths are identical, and also the separation between the black and red lattice points is finely tuned away from a distance of one-quarter wavelength: $d=0.25a+0.007a$; black hole: $A_{PC}=0.045a^2$, $c=0.45$, $h_{PC}=180$ nm; red hole: $A_{PC}=0.035a^2$, $c=1.0$, $h_{PC}=180$ nm. **b**, Calculated electric field distribution of the fundamental and first high-order modes of the single-lattice and double-lattice (structures II and III) resonators, where a circular resonator with a diameter of $L=200$ μm is considered. α_{0th} and α_{1st} are the total threshold gain of the fundamental and first high-order modes, respectively. **c**, Calculated threshold gain difference $\Delta\alpha$ as a function of resonator diameter L for structures I–III. Calculations for the single-lattice photonic crystal[28] are shown for comparison.

indicated in the left panel. The DBR structure, which is composed of 14 pairs of $Al_{0.1}Ga_{0.9}As/Al_{0.9}Ga_{0.1}As$ layers, is seen to be properly formed beneath the photonic crystal. We completed the device by bonding the laser chip to a thermally conductive submount and the submount to a water-cooled package. Images of the final assembly are shown in Fig. 4b. The wires shown in the inset of Fig. 4b are bonded to a ring-window electrode with an inner diameter of 900 μm on the n-side of the laser chip.

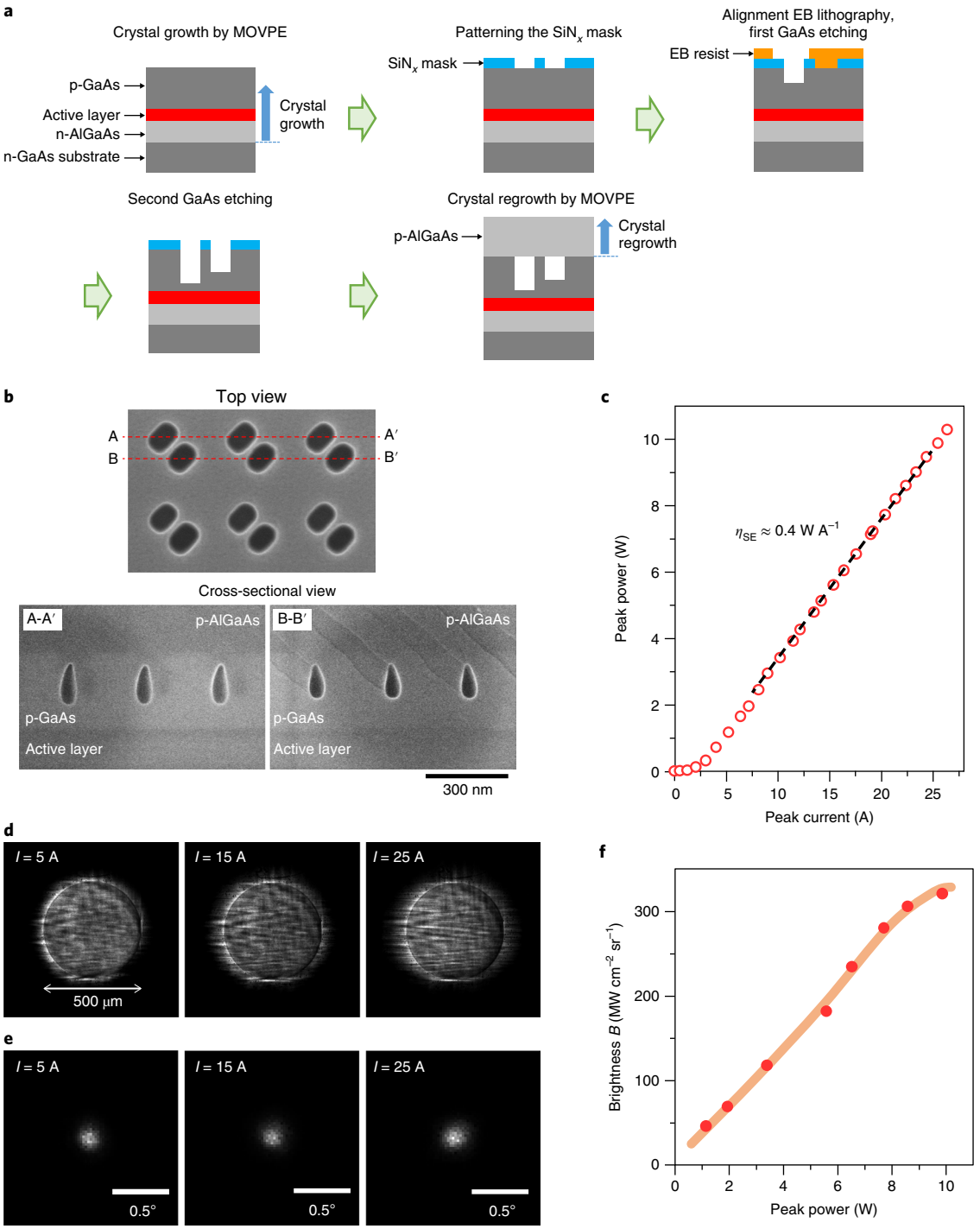

Fig. 3 | Process flow for fabricating double-lattice photonic crystals and lasing characteristics of the laser device under room-temperature, pulsed conditions. a, Schematic of device fabrication using a metal–organic vapour phase epitaxy (MOVPE) regrowth technique[31] and a two-step etching process. The two-step etching process is used to control the air-hole height difference independently of their relative in-plane size. **b**, Top and cross-sectional SEM images of the fabricated double-lattice photonic crystal using structure II before and after MOVPE regrowth. **c**, Output power as a function of peak injection current. The pulse width and repetition frequency were set to ~200 ns and 200 Hz, respectively. **d**, Measured NFP at different injection currents. Broad-area coherent lasing is observed over the 500-μm-diameter circular region. **e**, Measured FFP at different injection currents. A very narrow $1/e^2$ divergence angle of less than 0.3° is obtained due to broad-area coherent lasing. **f**, Laser brightness evaluated using the measured NFP and FFP widths. A very high brightness exceeding 300 MW cm^{-2} sr^{-1} is obtained.

Figure 4c shows output power versus injection current for the device under c.w. operation. The device was cooled by water at 5–20 °C during measurements. The threshold current was ~3.3 A, and the slope efficiency was ~0.48 W A^{-1} (as indicated by the dashed line). A high c.w. output power of up to ~7 W was obtained. Figure 4d shows a typical NFP of this device. The uniformity of the NFP was found to be degraded compared with that of the previous laser (Fig. 3d). This degradation of uniformity may originate from the degradation

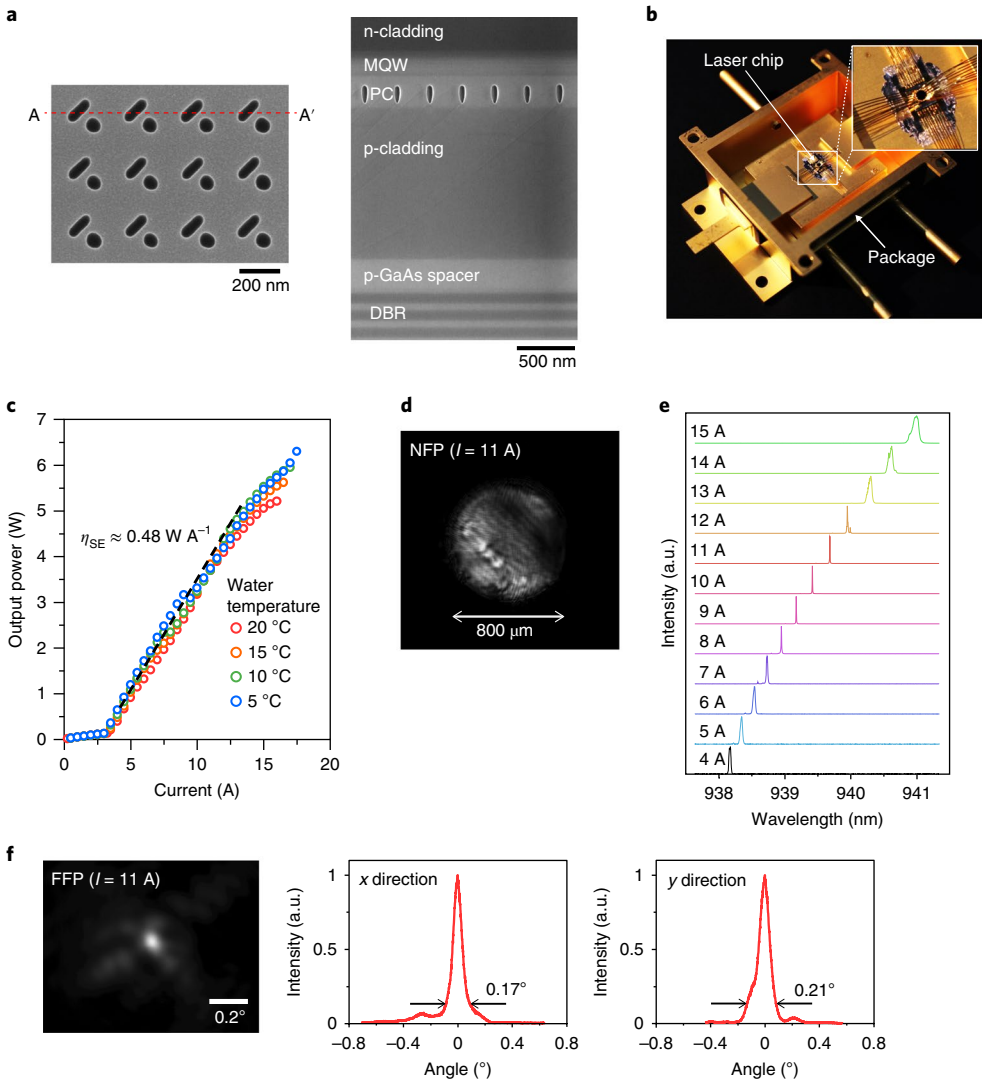

Fig. 4 | Lasing characteristics of the double-lattice photonic-crystal laser under c.w. conditions. a, Left, top-view SEM image of a double-lattice photonic crystal using structure III. Right, cross-sectional SEM image of the photonic-crystal air holes embedded by crystal regrowth. The cross-sectional view corresponds to the A–A′ line drawn in **a**. A DBR structure is introduced as a back reflector beneath the photonic crystal. **b**, Images of the laser chip bonded to a thermally conductive submount and a water-cooled package with its p-side down. The wires shown in the inset are bonded to a ring-window electrode on the n-side of the laser chip. **c**, Output power versus injection current under c.w. operation, where the device is cooled by water at temperatures of 5–20 °C during measurements. A high c.w. output power of up to ~7 W is obtained. **d**, NFP of the device at an injection current of 11 A. **e**, Lasing spectrum measured at various injection currents. A narrow spectral width is observed, particularly at injection currents of 8–11 A, where a single resonant peak is obtained. **f**, Measured FFP at an injection current of 11 A. Very narrow beam divergence angles of 0.17° along the *x* direction and 0.21° along the *y* direction (evaluated using the beam's $1/e^2$ width) are obtained. Measurements in **d**–**f** are taken at a water temperature of 20 °C.

of drawing accuracy during the electron beam lithography process, as described in the Methods. In addition, the presence of a temperature distribution within the photonic-crystal plane during c.w. operation is expected to have adversely affected the light confinement properties of the resonant wave. Nevertheless, as shown in the lasing spectra over a range of injection currents for a cooling water temperature of 20 °C (Fig. 4e), the spectral width is extremely narrow compared to typical broad-area, c.w. Fabry–Perot lasers, particularly at injection currents of 8–11 A (corresponding to output powers of 2.2–3.7 W), where a single resonant peak is obtained. In this single-mode region, the spectral width was measured to be 7 pm (evaluated by full-width at half-maximum, FWHM), which is limited by the spectral resolution of our spectrometer. In addition, as shown in the FFP (Fig. 4f), a very narrow beam divergence angle of 0.17° along the *x* direction and 0.21° along the *y* direction (evaluated using the beam's $1/e^2$ width) were obtained at an injection current of 11 A (corresponding to an output power of 3.7 W), which is very close to the diffraction limit of the 800 μm device. The c.w. laser brightness evaluated using the measured NFP and FFP widths at 11 A was ~180 MW cm^{-2} sr^{-1}. These results clearly indicate that the double-lattice photonic-crystal resonators are useful for realizing high-brightness lasers, even under c.w. conditions.

Optimized double-lattice photonic-crystal resonators

Here, we evaluate the theoretical maximum brightness expected using double-lattice photonic crystals, and by extension semiconductor lasers as a whole. With Fig. 1a, we explained that the double-lattice structure causes the 180°-diffracted light waves to interact destructively, relaxing the confinement of light throughout the entire structure and hence suppressing the oscillation of high-order

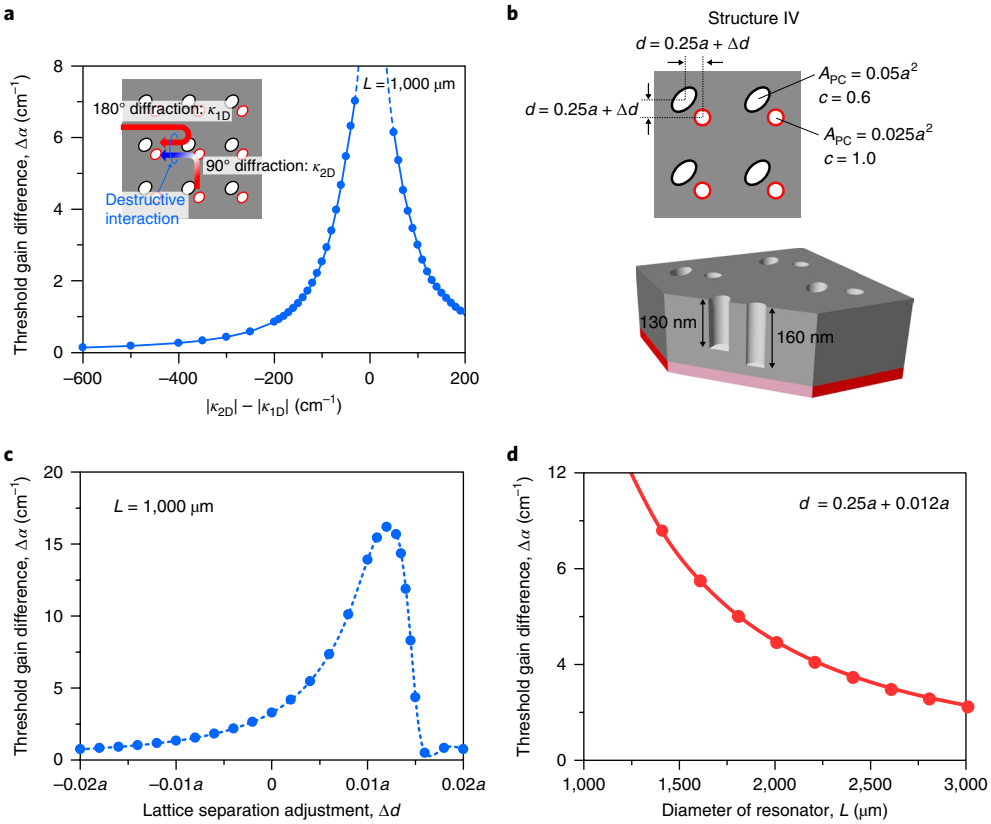

Fig. 5 | Optimized double-lattice photonic-crystal resonators using destructive interaction between 180°- and 90°-diffracted light waves. a, Threshold gain difference $\Delta\alpha$ between the fundamental and first high-order modes calculated as a function of $|\kappa_{2D}| - |\kappa_{1D}|$, where $|\kappa_{2D}|$ is set to 200 cm^{-1} and $|\kappa_{1D}|$ is varied. The phase difference between κ_{1D} and κ_{2D} is set to π to achieve destructive interaction of the light waves. $\Delta\alpha$ diverges when $|\kappa_{2D}| - |\kappa_{1D}| = 0$. Inset, schematic of destructive interaction between 180°- and 90°-diffracted light waves. **b**, Double-lattice photonic crystal, which we refer to as structure IV, with lattice separation $d = 0.25a + \Delta d$; black hole: $A_{PC} = 0.05a^2$, $c = 0.6$, $h_{PC} = 130$ nm; red hole: $A_{PC} = 0.025a^2$, $c = 1.0$, $h_{PC} = 160$ nm. **c**, Threshold gain difference $\Delta\alpha$ calculated as a function of lattice separation adjustment Δd using structure IV, where the resonator diameter is set to $L = 1{,}000\,\mu$m. A large $\Delta\alpha$ is obtained at around $\Delta d = 0.012a$ due to destructive interaction of the 180°- and 90°-diffracted light waves (that is, the balancing of κ_{1D} and κ_{2D}). **d**, Threshold gain difference $\Delta\alpha$ of structure IV as a function of the resonator diameter when $\Delta d = 0.012a$. As a result of the more complete destructive interaction of light, a sufficiently wide $\Delta\alpha$ is maintained up to a diameter of 2,500 μm.

modes. Now, we shall demonstrate that high-order modes can be suppressed further by causing not only the 180°-diffracted waves, but also the 90°-diffracted waves to interact destructively, as illustrated in the inset of Fig. 5a.

The effect of interaction between 180°- and 90°-diffracted light waves can be expressed by the difference of the coupling coefficients κ_{1D} and κ_{2D}. Figure 5a shows the threshold gain difference $\Delta\alpha$ between the fundamental and first high-order modes calculated as a function of the difference of κ_{1D} and κ_{2D} (that is, $|\kappa_{2D}| - |\kappa_{1D}|$). The phase difference between κ_{1D} and κ_{2D} is set to π to achieve destructive interaction of the 180°- and 90°-diffracted light waves. Evidently, $\Delta\alpha$ diverges when $|\kappa_{2D}| - |\kappa_{1D}| = 0$. This result indicates that we must use a photonic crystal with κ_{1D} and κ_{2D} values that are equal in magnitude but differ by π in phase in order to suppress the oscillation of high-order modes.

The balancing of κ_{1D} and κ_{2D} is possible by using the separation between the two lattice groups of the double-lattice photonic crystal as an additional degree of freedom. Through careful adjustment of the lattice-group separation from the nominal value of one-quarter wavelength, it is possible to tailor the strength and phase of the 180°-diffracted wave such that it destructively interacts with the 90°-diffracted waves. Let us define this separation adjustment as Δd. Figure 5b shows a new double-lattice photonic crystal, which we refer to as structure IV hereon, with lattice separation $d = 0.25a + \Delta d$, where $a \approx \lambda$. For values of Δd above (below) zero, the phase difference between κ_{1D} and κ_{2D} increases (decreases), leading to greater destructive (constructive) interaction. At around $\Delta d = 0.012a$, the two waves have nearly equal intensity and a π phase difference, resulting in their nearly complete destructive interaction, so $\Delta\alpha$ becomes very large, as shown in Fig. 5c. (Note that structure III in Fig. 2a also had an adjusted Δd so that sufficient destructive interaction was achieved up to a resonator diameter of 800 μm.) Details of the foregoing calculations are provided in Supplementary Section 5.

Figure 5d shows the threshold gain difference $\Delta\alpha$ of structure IV as a function of the resonator diameter when $\Delta d = 0.012a$. As a result of the more complete destructive interaction of light, structure IV exhibits a sufficiently wide $\Delta\alpha$ up to a diameter of 2,500 μm. This suggests that single- (or few-) mode operation is obtainable with a resonator of an area over several tens of times greater than those of the fabricated devices presented in Figs. 3 and 4. Such a broad-area semiconductor laser is expected to yield a brightness on the order of 1–10 GW cm^{-2} sr^{-1}. This evaluation foretells a future in which compact, affordable semiconductor lasers supplant bulky carbon dioxide and fibre/disk lasers as the definitive source of bright, coherent light.

Summary and outlook

We have proposed the concept of a double-lattice photonic-crystal resonator. This unique photonic crystal is capable of relaxing the

in-plane confinement of light, thereby enabling single- (or few-) mode operation of a photonic-crystal laser with a large emission area and high brightness. We have demonstrated an output power of 10 W with very narrow beam divergence angles of less than 0.3° in the x and y directions from a circular emission area of 500 μm diameter under pulsed conditions, which corresponds to a brightness of over 300 MW cm^{-2} sr^{-1}. The high brightness and narrow, symmetric beam produced by this resonator under pulsed conditions will aid in the development of compact, lens-free sources for LiDAR applications. In addition, under c.w. conditions, an output power of up to ~7 W and a brightness of ~180 MW cm^{-2} sr^{-1} have been obtained. Detailed theoretical calculations have revealed the possibility of an optimized double-lattice photonic crystal achieving an emission area several tens of times broader than those of the lasers fabricated here and a brightness of up to 10 GW cm^{-2} sr^{-1}. With its high brightness, achieved not by external optics but rather by its innately narrow divergence angle, the double-lattice photonic-crystal laser is expected to usher in an era in which technologies, including various sensing and material processing (for example, surface processing, welding, soldering and metal cutting) applications, are implemented using a single compact, affordable semiconductor chip. Other technologies that will benefit from these laser sources include medicine, lighting, projection displays and free-space wireless telecommunication and energy transmission.

Online content

Any methods, additional references, Nature Research reporting summaries, source data, statements of data availability and associated accession codes are available at https://doi.org/10.1038/s41563-018-0242-y.

Received: 26 April 2018; Accepted: 6 November 2018;
Published online: 17 December 2018

References

1. Ross, T. S. & Latham, W. P. Appropriate measures and consistent standard for high energy laser beam quality. *J. Directed Energy* **2**, 22–58 (2006).
2. Shukla, P., Lawrence, J. & Zhang, Y. Understanding laser beam brightness: a review and new prospective in material processing. *Opt. Laser Technol.* **75**, 40–51 (2015).
3. Paschke, K. et al. High power and high spectral brightness in 1060 nm α-DFB lasers with long resonators. *Electron. Lett.* **39**, 369–370 (2003).
4. Lim, J. J. et al. Design and simulation of next-generation high-power, high-brightness laser diodes. *IEEE J. Sel. Topics Quantum Electron.* **15**, 993–1008 (2009).
5. Crump, P. et al. Efficient high-power laser diodes. *IEEE J. Sel. Top. Quantum Electron.* **19**, 1501211 (2013).
6. Treusch, H.-G. et al. High-brightness semiconductor laser sources for materials processing: stacking, beam shaping, and bars. *IEEE J. Sel. Top. Quantum Electron.* **6**, 601–614 (2000).
7. Li, H. et al. Reliable high-efficiency high-brightness laser diode bars at 940 nm. *Opt. Laser Technol.* **36**, 327–329 (2004).
8. Karow, M. M. et al. Efficient 600-W-laser bars for long-pulse pump applications at 940 and 975 nm. *IEEE Photon. Technol. Lett.* **29**, 1683–1686 (2017).
9. Miah, M. J. et al. 1.9 W continuous-wave single transverse mode emission from 1060 nm edge-emitting lasers with vertically extended lasing area. *Appl. Phys. Lett.* **105**, 151105 (2014).
10. Gründl, T. et al. Record single-mode, high-power VCSELs by inhibition of spatial hole burning. *IEEE J. Sel. Top. Quantum Electron.* **19**, 1700913 (2013).
11. Seurin, J.-F. et al. High-brightness pump sources using 2D VCSEL arrays. *Proc. SPIE* **7615**, 76150F (2010).
12. Siegman, A. E. New developments in laser resonators. *Proc. SPIE* **1224**, 2–14 (1990).
13. Chang-Hasnain, C. J. et al. Transverse mode characteristics of vertical cavity surface-emitting lasers. *Appl. Phys. Lett.* **57**, 218–220 (1990).
14. Siegman, A. E. Defining, measuring, and optimizing laser beam quality. *Proc. SPIE* **1868**, 2–12 (1993).
15. Wenzel, H.et al. Theoretical and experimental analysis of the lateral modes of high-power broad-area lasers. *Proceedings of Numerical Simulation of Optoelectronic Devices (NUSOD)* 143–144 (2011).
16. Crump, P. et al. Experimental and theoretical analysis of the dominant lateral waveguiding mechanism in 975 nm high power broad area diode lasers. *Semicond. Sci. Technol.* **27**, 045001 (2012).
17. Winterfeldt, M., Crump, P., Wenzel, H., Erbert, G. & Tränkle, G. Experimental investigation of factors limiting slow axis beam quality in 9xx nm high power broad area diode lasers. *J. Appl. Phys.* **116**, 063103 (2014).
18. Sverdlov, B. et al. Optimization of fiber coupling in ultra-high power pump modules at λ=980nm. *Proc. SPIE* **8605**, 860508 (2013).
19. Sumpf, B. et al. High-brightness quantum well tapered lasers. *IEEE J. Sel. Topics Quantum Electron.* **13**, 1009–1020 (2009).
20. Imada, M., Noda, S., Chutinan, A. & Tokuda, T. Coherent two-dimensional lasing action in surface-emitting laser with triangular-lattice photonic crystal structure. *Appl. Phys. Lett.* **75**, 316–318 (1999).
21. Riechel, S., Kallinger, C., Lemmer, U. & Feldmann, J. A nearly diffraction limited surface emitting conjugated polymer laser utilizing a two-dimensional photonic band structure. *Appl. Phys. Lett.* **77**, 2310–2312 (2000).
22. Noda, S., Yokoyama, M., Imada, M., Chutinan, A. & Mochizuki, M. Polarization mode control of two-dimensional photonic crystal laser by unit cell structure design. *Science* **293**, 1123–1125 (2001).
23. Ryu, H.-Y., Kwon, S.-H., Lee, Y.-J., Lee, Y.-H. & Kim, J.-S. Very-low-threshold photonic band-edge lasers from free-standing triangular photonic crystal slabs. *Appl. Phys. Lett.* **80**, 3476–3478 (2002).
24. Miyai, E. et al. Lasers producing tailored beams. *Nature* **441**, 946 (2006).
25. Kim, M. et al. Surface-emitting photonic-crystal distributed-feedback laser for the midinfrared. *Appl. Phys. Lett.* **88**, 191105 (2006).
26. Matsubara, H. et al. GaN photonic-crystal surface-emitting laser at blue-violet wavelengths. *Science* **319**, 445–447 (2008).
27. Kurosaka, Y. et al. On-chip beam-steering photonic-crystal lasers. *Nat. Photon.* **4**, 447–450 (2010).
28. Hirose, K. et al. Watt-class high-power, high-beam-quality photonic crystal lasers. *Nat. Photon.* **8**, 406–411 (2014).
29. Liang, Y., Peng, C., Sakai, K., Iwahashi, S. & Noda, S. Three-dimensional coupled-wave model for square-lattice photonic crystal lasers with transverse electric polarization: a general approach. *Phys. Rev. B* **84**, 195119 (2011).
30. Liang, Y., Peng, C., Sakai, K., Iwahashi, S. & Noda, S. Three-dimensional coupled-wave analysis for square-lattice photonic-crystal lasers with transverse electric polarization: finite-size effects. *Opt. Express* **20**, 15945–15961 (2012).
31. Yoshida, M. et al. Fabrication of photonic-crystal structures by tertiary-butyl arsine-based metal–organic vapor-phase epitaxy for photonic-crystal lasers. *Appl. Phys. Express* **9**, 062702 (2016).

Acknowledgements

This work was supported by the ACCEL programme commissioned by the Japan Science and Technology Agency (JST) and the Photon Frontier Network Program of the Ministry of Education, Culture, Sports, Science and Technology (MEXT), and is supported by the New Energy and Industrial Technology Development Organization (NEDO). M.Y. also acknowledges support by a Grant-in-Aid for JSPS Fellows. The authors thank S. Yagi, H. Kitagawa, A. Watanabe, E. Miyai, and W. Kunishi for fruitful discussions.

Author contributions

S.N. designed and directed this work. M.Y. fabricated the device with K.I. and M.D.Z. M.Y. measured the lasing characteristics with M.K. Y.T. and J.G. conducted the theoretical analysis of the device. H.R. performed epitaxial growth for the device. M.D.Z and B.S assembled the device. M.Y. wrote the manuscript with S.N. and J.G.

Competing interests

The authors declare no competing interests.

Additional information

Supplementary information is available for this paper at https://doi.org/10.1038/s41563-018-0242-y.

Reprints and permissions information is available at www.nature.com/reprints.

Correspondence and requests for materials should be addressed to S.N.

Publisher's note: Springer Nature remains neutral with regard to jurisdictional claims in published maps and institutional affiliations.

Methods

Device fabrication. The device was fabricated using a MOVPE regrowth technique and a two-step etching process as shown in Fig. 3a. First, we grew an n-AlGaAs cladding layer, an active layer (InGaAs/AlGaAs multiple quantum wells), an AlGaAs carrier blocking layer and a p-GaAs layer into which the photonic crystal pattern is transferred. Next, we deposited a hard (SiN_x) etch mask onto the p-GaAs layer, then transferred the double-lattice pattern onto this mask by electron beam lithography and SF_6 inductively coupled plasma (ICP) etching. During the electron beam writing process, drawing accuracy was ensured by fixing the sample stage and exposing the entire pattern by only deflecting the electron beam. Next, we covered the etch mask in electron beam resist and exposed only one of the two holes using alignment electron beam lithography, then etched the exposed hole to a desired depth of a few tens of nanometres using HI/Xe ICP etching. Afterward, we removed the electron beam resist, then etched the two holes simultaneously by HI/Xe ICP etching, resulting in the formation of the final photonic crystal pattern. Before MOVPE regrowth, we removed the SiN_x mask using BHF, and then removed the surface oxide by soaking the sample in HCl. After these surface treatments, we loaded the sample into the MOVPE chamber and embedded the photonic crystal under a p-AlGaAs cladding layer and a p^+-GaAs contact layer by MOVPE regrowth. During regrowth, the V/III ratio was 10, the total pressure was 10 kPa, and the growth rate was 1 μm h^{-1}. The morphology of the regrown surface was smooth, to the same degree as the regrown surface of a sample without the photonic crystal. The surface roughness was found to be on the order of a monolayer. The root-mean-square (r.m.s.) roughness measured by atomic force microscopy was 0.31 nm, as shown in Supplementary Fig. 4. Then, a circular p-electrode with a diameter of 500 μm was deposited onto the p^+-GaAs contact layer, and a ring-window n-electrode with an inner diameter of 600 μm was deposited onto the n-GaAs substrate. Finally, the device was mounted with its p-side down.

The fabrication processes for the pulsed device in Fig. 3 ($L = 500$ μm) and the c.w. device in Fig. 4 ($L = 800$ μm) differed in their electron beam writing processes. Unlike the photonic crystal of the pulsed device, the 800 μm photonic crystal of the c.w. device exceeded the exposure field of the electron beam, requiring the sample stage to be moved to write the entire pattern and thus resulting in a slight degradation of the drawing accuracy.

Reporting Summary. Further information on research design is available in the Nature Research Reporting Summary linked to this article.

Data availability

The data that support the findings of this study are available from the corresponding author upon reasonable request.

Corresponding Author Name: Susumu Noda

Manuscript Number: NM18041401A

Reporting checklist for manuscripts with a claim of lasing

In order to promote clarity in claims of lasing we strongly recommend that authors provide the following information when making a claim of lasing action in a new material or device design. We appreciate that in certain circumstances, e.g. random lasers and lasing from nanoscale areas, capturing all recommended data may not be feasible, but we encourage authors to provide the strongest evidence possible. **Please supply a response to the checklist alongside your submitted manuscript, and ensure that the relevant responses are also provided in the main manuscript, methods section or supplementary information as appropriate.** The completed checklist will be shared with reviewers.

Laser data:	Response
1. Have plots of device output power versus pump power been provided over a wide range of values, and do they show a clear threshold?	The plots of light output power versus injection current are provided over a wide range of currents from below threshold to I = 13Ith (pulsed operation, Fig. 3c) and I=5Ith (continuous-wave (CW) operation, Fig. 4c), where Ith is threshold current. These plots show a clear threshold as shown in Fig. 3c and Fig. 4c; detailed threshold values are provided in the answer to Question 5.
2. Have plots of spectral power density for the emission been provided at pump powers below, around and above threshold and do they indicate clear linewidth narrowing of the emission at the lasing transition? Please state the resolution of the spectrometer used to make the measurements.	Plots of the lasing spectrum above threshold are provided in the manuscript. We can also provide spectra below and around threshold if necessary. We have observed clear linewidth narrowing of the emission at the lasing transition. The resolution of our spectrometer is 7 pm as described in the manuscript (page 19, lines 319-321).
3. Has the coherence or polarization of the laser emission been measured?	We have provided far-field patterns exhibiting narrow beam divergence (<0.3°), corresponding to nearly diffraction-limited beam quality, which clearly indicate that the laser emission is coherent. We have also measured the polarization of the laser beam and confirmed that the polarization is as designed.
4. Has the spatial profile of the emission been measured or imaged, and does it indicate the existence of a well-defined beam above threshold?	The spatial profile (near- and far-field images) of the emission beam has been measured using a CCD camera and clearly shows the existence of a well-defined beam. These measurements are shown in Figs. 3d, 3e, 4d and 4f.
5. Please ensure the pumping conditions (continuous-wave, pulsed, temperature of operation) are clearly stated in the manuscript. In particular, please ensure that threshold values are provided as a density value e.g. W cm^{-2} or J cm^{-2} taking into the account the area of the device.	The pumping conditions are clearly stated in the manuscript (page 16, lines 266-267 for pulsed operation and page 18, lines 304-305 for CW operation). The threshold current densities are ~1.0kA/cm^2 (the device in Fig. 3 under pulsed operation) and ~0.66kA/cm^2 (another device in Fig. 4 under CW operation).

(Continues on following page)

Laser data:

	Response
6. Have alternative explanations, e.g. amplified spontaneous emission, directional scattering, modification of fluorescence spectrum by cavity, been ruled out as being responsible for the emission characteristics?	Our measurements show a clear threshold, a narrow spectral linewidth, and narrow beam divergence. These measurements clearly indicate that lasing action has been obtained, so we have not provided alternative explanations.
7. Has theoretical analysis been performed to ensure that the experimental values measured for characteristics such as laser threshold, linewidth, cavity gain–loss and laser efficiency are realistic and reasonable?	A theoretical analysis based on coupled-wave theory has been performed as described in the manuscript and the supplementary information. The lasing mode and cavity loss obtained therein are reasonable. Although not shown in the manuscript in detail, other theoretical results such as lasing wavelength, output efficiency, beam pattern are also in agreement with the experimental ones.
8. How many devices have been fabricated and tested? Can you provide statistics for their behaviour (e.g. time before failure), and estimate any errors that may be present?	For pulsed operation, we fabricated 38 devices. We tested four of these with the same design, and confirmed that their characteristics are almost identical (Figs. 3c-f). For CW operation, we fabricated 39 devices. Among these, we tested 7 devices, each with slightly different designs, and obtained ~7W output power for the best device (Fig. 4c-f), >4W for 2 others, and >2W for the remaining 4.

Further reading:

We also suggest that authors read the following literature, which describes the important principles and signatures of laser emission, and also discusses some of the common mistakes that can occur during laser characterization.

1. Samuel, I. D. W., Namdas, E. B. & Turnbull, G. A. How to recognize lasing. *Nat. Photon.* **3,** 546–549 (2009).
2. Siegman, A. E. *Lasers* (University Science Books, 1990).
3. Svelto, O. *Principles of Lasers* 5th edn (Springer, 2010).
4. Blood, P. *Quantum Confined Laser Devices: Optical Gain and Recombination in Semiconductors* (Oxford Univ. Press, 2015).
5. Kozlov, V. G., Bulović, V., Burrows, P. E. & Forrest, S. R. Laser action in organic semiconductor waveguide and double-heterostructure devices. *Nature* **389,** 362–364 (1997).

Nature Research, brought to you courtesy of Springer Nature Limited (“Nature Research”)

Terms and Conditions

Nature Research supports a reasonable amount of sharing of content by authors, subscribers and authorised or authenticated users (“Users”), for small-scale personal, non-commercial use provided that you respect and maintain all copyright, trade and service marks and other proprietary notices. By accessing, viewing or using the nature content you agree to these terms of use (“Terms”). For these purposes, Nature Research considers academic use (by researchers and students) to be non-commercial.

These Terms are supplementary and will apply in addition to any applicable website terms and conditions, a relevant site licence or a personal subscription. These Terms will prevail over any conflict or ambiguity with regards to the terms, a site licence or a personal subscription (to the extent of the conflict or ambiguity only). By sharing, or receiving the content from a shared source, Users agree to be bound by these Terms.

We collect and use personal data to provide access to the nature content. ResearchGate may also use these personal data internally within ResearchGate and share it with Nature Research, in an anonymised way, for purposes of tracking, analysis and reporting. Nature Research will not otherwise disclose your personal data unless we have your permission as detailed in the Privacy Policy.

Users and the recipients of the nature content may not:

1. use the nature content for the purpose of providing other users with access to content on a regular or large scale basis or as a means to circumvent access control;
2. use the nature content where to do so would be considered a criminal or statutory offence in any jurisdiction, or gives rise to civil liability, or is otherwise unlawful;
3. falsely or misleadingly imply or suggest endorsement, approval , sponsorship, or association unless explicitly agreed to by either Nature Research or ResearchGate in writing;
4. use bots or other automated methods to access the nature content or redirect messages; or
5. override any security feature or exclusionary protocol.

These terms of use are reviewed regularly and may be amended at any time. We are not obligated to publish any information or content and may remove it or features or functionality at our sole discretion, at any time with or without notice. We may revoke this licence to you at any time and remove access to any copies of the shared content which have been saved.

Sharing of the nature content may not be done in order to create substitute for our own products or services or a systematic database of our content. Furthermore, we do not allow the creation of a product or service that creates revenue, royalties, rent or income from our content or its inclusion as part of a paid for service or for other commercial gain. Nature content cannot be used for inter-library loans and librarians may not upload nature content on a large scale into their, or any other, institutional repository.

To the fullest extent permitted by law Nature Research makes no warranties, representations or guarantees to Users, either express or implied with respect to the nature content and all parties disclaim and waive any implied warranties or warranties imposed by law, including merchantability or fitness for any particular purpose.

Please note that these rights do not automatically extend to content, data or other material published by Nature Research that we license from third parties.

If you intend to distribute our content to a wider audience on a regular basis or in any other manner not expressly permitted by these Terms please contact us at

onlineservice@springernature.com